

Direct numerical simulation of sharkskin denticles in turbulent channel flow

A. Boomsma and F. Sotiropoulos^{*}

Citation: [Phys. Fluids](#) **28**, 035106 (2016); doi: 10.1063/1.4942474

View online: <http://dx.doi.org/10.1063/1.4942474>

View Table of Contents: <http://aip.scitation.org/toc/phf/28/3>

Published by the American Institute of Physics

Direct numerical simulation of sharkskin denticles in turbulent channel flow

A. Boomsma¹ and F. Sotiropoulos^{2,a)}

¹Department of Mechanical Engineering, University of Minnesota, Minneapolis, Minnesota 55414, USA

²Department of Civil Engineering, College of Science and Engineering, Stony Brook University, Stony Brook, New York 11794, USA

(Received 2 December 2015; accepted 22 January 2016; published online 15 March 2016)

The hydrodynamic function of sharkskin has been under investigation for the past 30 years. Current literature conflicts on whether sharkskin is able to reduce skin friction similar to riblets. To contribute insights toward reconciling these conflicting views, direct numerical simulations are carried out to obtain detailed flow fields around realistic denticles. A sharp interface immersed boundary method is employed to simulate two arrangements of actual sharkskin denticles (from *Isurus oxyrinchus*) in a turbulent boundary layer at $Re_\tau \approx 180$. For comparison, turbulent flow over drag-reducing scalloped riblets is also simulated with similar flow conditions and with the same numerical method. Although the denticles resemble riblets, both sharkskin arrangements increase total drag by 44%-50%, while the riblets reduce drag by 5%. Analysis of the simulated flow fields shows that the turbulent flow around denticles is highly three-dimensional and separated, with 25% of the total drag being form drag. The complex three-dimensional shape of the denticles gives rise to a mean flow dominated by strong secondary flows in sharp contrast with the mean flow generated by riblets, which is largely two-dimensional. The so resulting three-dimensionality of sharkskin flows leads to an increase in the magnitude of the turbulent statistics near the denticles, which further contributes to increasing the total drag. The simulations also show that, at least for the simulated arrangements, sharkskin, in sharp contrast with drag-reducing riblets, is unable to isolate high shear stress near denticle ridges causing a significant portion of the denticle surface to be exposed to high mean shear. © 2016 AIP Publishing LLC. [<http://dx.doi.org/10.1063/1.4942474>]

I. INTRODUCTION

A. Background information

Sharkskin is comprised of small tooth-like structures called denticles, or placoid scales which are affixed to a flexible epidermis/membrane. Fluid dynamicists and biologists have been attempting to elucidate the function of denticles over the past 30 years. In 1986, Raschi and Musick¹ took sharkskin samples from 15 species and measured denticles from different shark-body regions. A denticle taken from *Carcharhinus leucas* is shown in Figure 1. The primary keel (i.e., ridge) is labeled, and this particular denticle has secondary and tertiary keels. Sharkskin denticles are aligned parallel to the longitudinal axis of the shark and are directly exposed to water.

Raschi and Musick¹ theorized that denticles might behave similarly to riblets. Riblets are micro-grooved structures (on the order of 100 μm wide) that are aligned in the primary direction of fluid flow. Riblets have seen a rich history of research, which has proven their effectiveness to passively reduce skin-friction up to 10%.² Experimental results for a variety of riblet shapes and sizes can be found in publications by Walsh³ and Bechert *et al.*² Traditionally, drag reduction by

^{a)}Electronic mail: fotis.sotiropoulos@stonybrook.edu

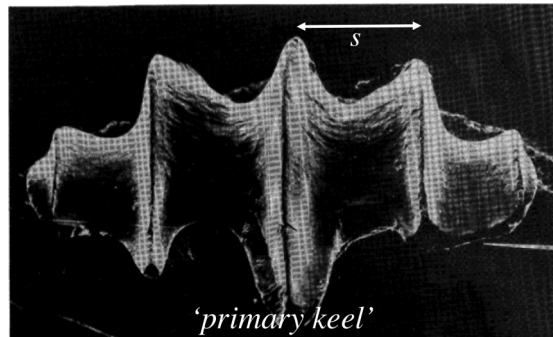


FIG. 1. Denticle from *Carcharhinus leucas*. Width between keels, s , with the primary keel being centered. From Raschi and Musick, *Hydrodynamic Aspects of Shark Scales*. Copyright 1986 National Aeronautics and Space Administration. Reproduced with permission from NASA-CR-3963.

riblets is plotted as a function of riblet width (plotted in wall coordinates), $s^+ = sw_{\tau,0}/\nu$, where the friction velocity, $w_{\tau,0} = \sqrt{\tau_0/\rho}$, is based on τ_0 , which is the wall shear stress on the surface without riblets. Although the optimum width for drag reduction varies with shape, in general, riblets achieve maximum drag reduction at a size near $s^+ \approx 15$.

To understand the mechanisms of drag reduction by riblets, several experimental papers (e.g., Djenidi and Antonia,⁴ Park and Wallace,⁵ Lee and Lee,⁶ Suzuki and Kasagi⁷) have examined the structure of turbulence very near riblets. Computational studies by Choi *et al.*,⁸ Chu and Karniadakis,⁹ and Goldstein *et al.*¹⁰ endeavored to clarify these mechanisms with Direct Numerical Simulation (DNS). Together, these publications have confirmed that drag-reducing riblets decrease RMS velocity fluctuations near the riblets by prohibiting larger scales of turbulence from interacting with much of the riblet surface area. This in turn isolates high shear stress regions to the very tips of the riblets.

Raschi and Musick¹ made the comparison between riblets and sharkskin because denticles have a cross-sectional shape similar to scalloped riblets. Furthermore, when denticles overlap each other, this cross section is preserved in the streamwise direction, further resembling riblets. Figure 2 shows a top view of sharkskin from a bonnethead shark. Although the riblets and sharkskin look alike, the true test of whether they *act alike* is whether or not sharkskin can inhibit turbulent mixing, which is critical in reducing drag.

As mentioned, the best predictor of whether or not sharkskin can reduce skin-friction is the width between keels in wall units, or s^+ . The width between denticle keels was easily measured by Raschi and Musick,¹ but the value of $w_{\tau,0}$ was unknown. These authors approximated this value using canonical flat-plate turbulent boundary layer relations—an approximation that does not

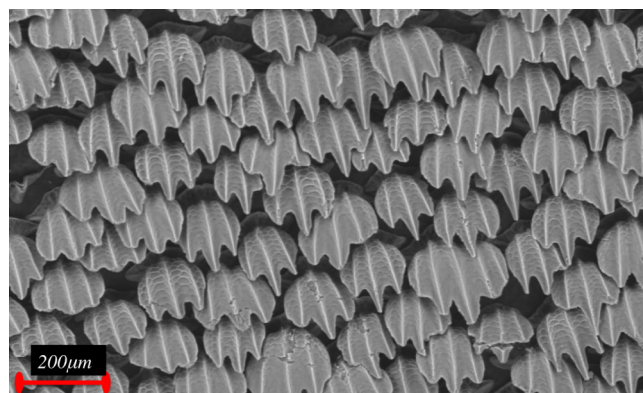


FIG. 2. Top view of sharkskin from *Sphyrna tiburo*. Reproduced with permission from George Lauder. Copyright 2014, Lauder Laboratory, Harvard University.

incorporate any pressure gradient or roughness effects. In any case, the approximation led Raschi and Musick¹ to conclude that at voluntary swimming speeds (≈ 55 cm/s), the denticle spacing was only $s^+ \approx 1.5$. This s^+ value is much lower than the optimal value for scalloped riblets, $s^+ \approx 16$ (see Bechert *et al.*²), so denticles at voluntary speeds would be suspected to be of little consequence. However, at burst swimming speeds (≈ 1000 cm/s), the authors calculate that for fast-swimming (e.g., *Isurus oxyrinchus*) species of shark, $s^+ \approx 13\text{--}15$, which supports the theory that sharkskin is meant to passively reduce drag.

With the aforementioned commonalities aside, there are three crucial differences between denticles and riblets. First, the shape of denticles is highly three-dimensional while riblets are two-dimensional. Second, riblets retain a constant cross-sectional area in the streamwise direction, which is definitely not always the case with sharkskin. In fact, the degree to which denticles overlap has not been quantified. It is a function of species and the location on the animal's body. Figure 2 shows a bed of denticles that are not tightly packed, but other species (see Reif and Bechert¹¹) do have denticles that interlock with each other more. Third, each denticle has the ability to bristle (see Lang *et al.*¹²), or tilt away/towards the epidermis at some Angle of Incidence (AOI). Denticle bristling adds a three-dimensionality that riblets would never introduce.

B. Comparisons between sharkskin and riblets

Currently, there is no agreement in the literature as to whether sharkskin is hydrodynamically beneficial to the species (see the review by Dean and Bhushan¹³). In 1985, Reif *et al.*¹¹ created a mold from actual sharkskin and tested it in an air channel. With this apparatus, the authors were able to examine skin-friction at many values of denticle s^+ . At two values of AOI (5° and 10°), they found that denticles *increased* drag. It should be noted though that the mold was not a replica because it did not contain cavities under the denticles. Later, in 2000, Bechert *et al.*¹⁴ created more realistic denticle models and tested them in an oil channel. When the denticles were perfectly interlocked, drag reduction occurred but, as in the previous study, at an AOI the sharkskin increased skin-friction drag. A conclusion from both of these experiments is that the *three-dimensionality of the denticles is detrimental to drag reduction*.

There is however some experimental evidence that sharkskin can reduce drag. Jung and Bhushan¹⁵ created milled denticles (*Squalus acanthias*) and tested them in a micro-channel (hydraulic diameter of 1 mm). They found a 30% reduction in pressure drop compared to a smooth surface. Oeffner and Lauder¹⁶ tested actual sharkskins from *Isurus oxyrinchus* and *Lamna nasus* in a water channel. In this work, the skins were mounted on a flat plate that was heaved and pitched to propel the plate upstream at some self swimming speed (SSP). Oeffner and Lauder¹⁶ found that sharkskin mounted on rigid plates decreased the SSP of the test section (suggesting an increase in drag). However, when the same sharkskin was mounted on a flexible plate, an increase in SSP of $\approx 12\%$ occurred on average. More recently, Wen and Lauder¹⁷ used a three-dimensional printer to create detailed denticles (*Isurus oxyrinchus*) on a substrate. When immersed in a water channel, these authors found that the denticles behaved similarly to riblets, with a maximum drag reduction of about 9%.¹⁷

We argue that the existing experimental studies are conflicting and difficult to interpret because of three main reasons: (1) manufactured sharkskin may not accurately mimic real skin, (2) lack of consistency among the turbulent flows in which the sharkskin was exposed in each experiment, and (3) the lack of knowledge regarding the flow-field details in the vicinity of the denticles. Therefore, first goal of this work is to determine whether or not sharkskin denticles can passively reduce skin-friction similarly to riblets in a systematic approach. Second objective of our work is to elucidate the fundamental physical reason for either cases, which will hopefully shed light in the discrepancies in the literature. We undertake a series of DNS for various denticle arrangements using an immersed boundary (IB) method to simulate the complex geometry of sharkskin. We also undertake a DNS for scalloped riblets at similar flow conditions to enable direct comparisons between the riblet and denticle induced flow fields and drag reduction efficiency. While our work does incorporate simplifying assumptions, e.g., denticles are mounted on a rigid flat surface and their AOI is held fixed, our simulations are, to the best of our knowledge, the first to provide

detailed insights into the flow fields in the vicinity of denticles and identify specific mechanisms that contribute to the overall drag. The paper is organized as follows: in Section II we present an overview of the numerical method. We detail the computational domain in Section III. Section IV details the validation of the DNS solver. In Section V we discuss the present results and finally, we conclude in Section VI.

II. NUMERICAL METHODS

The turbulent flow in a channel is governed by the incompressible Navier-Stokes equations. The momentum equations and continuity equation have been partially transformed into generalized curvilinear coordinates and are shown in

$$J \frac{\partial U^j}{\partial \xi_j} = 0, \quad (1)$$

$$\frac{1}{J} \frac{\partial U^i}{\partial t} + \frac{\xi_m^i}{J} \frac{\partial}{\partial \xi_j} (U^j u_m) = \frac{\xi_m^i}{J} \left(\frac{1}{\rho} \frac{\partial}{\partial \xi_j} (\mu g^{jk} \frac{\partial u_m}{\partial \xi_k}) - \frac{1}{\rho} \frac{\partial}{\partial \xi_j} \left(\frac{\xi_m^j p}{J} \right) - \frac{1}{\rho} \frac{\partial \tau_{mj}}{\partial \xi_j} \right). \quad (2)$$

Here, the Jacobian of the transformation, J , is defined as $J = |\partial(\xi_1, \xi_2, \xi_3)/\partial(x_1, x_2, x_3)|$ and $\xi_m^i = \partial \xi_i / \partial x_m$ are the transformation metrics. Cartesian velocity components are given as u_m , and U^j is the contravariant volume flux. The static pressure is p , density is ρ , and the dynamic viscosity is μ . Finally, g^{jk} is the contravariant metric tensor and τ_{mj} is the stress tensor.

The governing equations are discretized on a hybrid staggered/non-staggered grid with three-point, central finite difference formulas and integrated in time via a second-order accurate fractional step method. The momentum equations are solved using an explicit fourth-order modified Runge-Kutta method. The Poisson equation for satisfying the discrete continuity equation is solved using algebraic multigrid for matrix conditioning along with the generalized minimum-residual method.¹⁸ All simulations reported in this paper are DNS and thus no turbulence closure is required.

To handle the arbitrary geometric complexity of a channel with a bed of denticles we employ the Curvilinear Immersed Boundary (CURVIB) method of Ge and Sotiropoulos.¹⁹ The surface of each denticle is discretized with an unstructured triangular mesh and embedded in a background Cartesian grid used to discretize the empty channel geometry. The basic idea of the method is illustrated in Figure 3. A background mesh cell is either identified as a node interior to the denticles (cells with an X), a fluid node (filled circles), or an IB node (open circles). Boundary conditions for the velocity components are reconstructed at the IB nodes using interpolation along the normal to the body originating from the IB node (see Figure 3). Assuming the grid is fine enough so that the IB nodes are located within the viscous sublayer, linear interpolation can be used to reconstruct velocity boundary conditions.

To calculate the drag force acting on the denticles we employ the method proposed by Borazjani and Sotiropoulos,²⁰ namely, integrating the pressure and viscous forces along the surface that

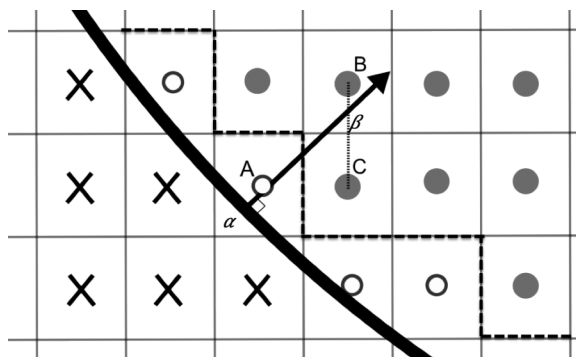


FIG. 3. IBM node classification and interpolation methods. Structure nodes (X), IB nodes (open circles), and fluid nodes (filled circles). Dashed line is the surface area where the viscous stress tensor is computed.

TABLE I. Computational domain details.

Case	L_x	L_z	Δx_{min}^+ , Δx_{max}^+	Δy_{min}^+ , Δy_{max}^+	Δz^+	$N_x \times N_y \times N_z$
Baseline	$3.20L_y$	$6.40L_y$	3.0	0.27, 3.9	7.0	$190 \times 150 \times 166$
Aligned	$2.96L_y$	$6.03L_y$	0.75	0.75, 3.3	0.75	$723 \times 123 \times 1466$
Staggered	$2.96L_y$	$6.25L_y$	0.75	0.75, 3.3	0.75	$720 \times 123 \times 1521$
Riblet	$3.04L_y$	$6.30L_y$	0.18, 1.5	0.24, 6.9	7.0	$1157 \times 104 \times 161$

approximates the IB interface as shown in Figure 3. We denote this as the denticle surface, Ω , and compute the flow imparted force on the denticle surface as follows:

$$F_i = \int_{\Omega} -pn_i d\Omega + \int_{\Omega} \tau_{ij}n_j d\Omega. \quad (3)$$

Here, n_i is the normal vector to a triangular element of the immersed body and τ_{ij} is the viscous stress tensor. The velocity derivatives required to calculate the components of the stress tensor are calculated using first order accurate differencing, which is accurate assuming that the IB nodes are all located within the laminar sublayer (see Table I for near-wall grid resolution of our simulations). To visualize the mean shear stress on an immersed body, we project τ_{ij} at the IB nodes onto the unstructured mesh of the immersed body by averaging the stress tensor from the nearest IB nodes.

III. TEST CASES AND COMPUTATIONAL DETAILS

Most computational studies concerning ripples have been performed in turbulent channel flow, so to make a direct comparison, we have chosen to simulate the denticles in a similar fashion. Following the works of Choi,⁸ Chu,⁹ and Garcia-Mayoral²¹ we have created a rectangular domain with a structured grid and filled the bottom with denticles as shown in Figure 4.

We have conducted simulations for two different denticle arrangements also shown in Figure 4. Depending upon the location of the denticles on the shark body, denticles can be very tightly or loosely packed, as shown by Wen and Lauder.¹⁷ The spacings chosen for this work mimic the arrangement shown in Figure 2 and is the same arrangement that was 3D printed by Wen and Lauder¹⁷ (for the aligned case). This arrangement is also useful in identifying the effects of the denticle crown; as previously mentioned, Bechert *et al.*¹⁴ was able to achieve drag reduction when denticles are interlocked and essentially two-dimensional. For both cases, a total of 324 individual denticles were used.

Periodic boundary conditions are employed in the spanwise (x) and streamwise (z) directions (velocity components u, v, w correspond to directions x, y, z). The denticles are attached to a static, no-slip surface. A stress-free boundary condition is applied on the top of the domain. In the baseline and sharkskin cases, a constant mass-flux is maintained in the streamwise direction equal to $L_y \cdot L_x$.

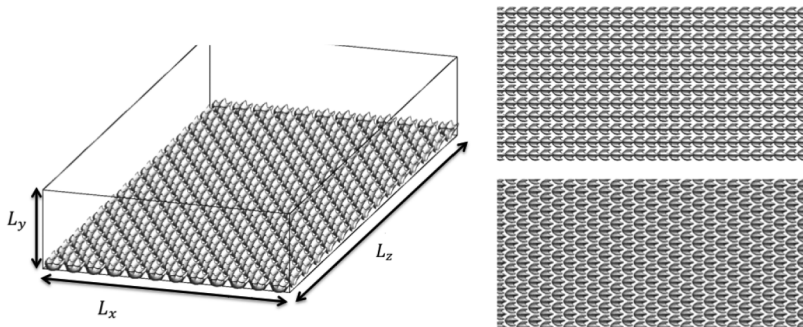


FIG. 4. Computational domain with staggered denticles and dimensions (left). Top views of aligned and staggered arrangements (right).

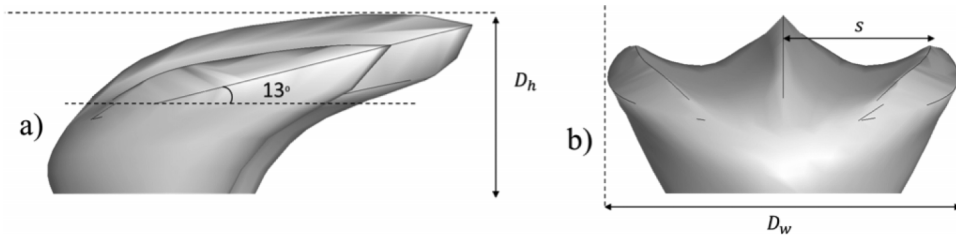


FIG. 5. Representative denticle from *Isurus oxyrinchus*. (a) YZ plane-view and (b) XY plane-view.

The baseline for this experiment is a similar domain without denticles. The Reynolds number is defined as $Re = \delta W_{bulk}/\nu$, where δ is the length of L_y , W_{bulk} is the integrated primary velocity, and ν is the kinematic viscosity. In the baseline simulation, $Re = 2800$, which correlates to $Re_\tau \approx 180$. When denticles are included in the domain, the viscosity remains unchanged. Domain sizes and cell counts are detailed in Table I—note that for every case, $L_y = 2$. For the baseline and sharkskin cases, the background grid is uniform in the spanwise and streamwise directions. A stretched grid is employed in the wall-normal direction. The resolutions for the various grids we employ are reported in Table I.

A representative denticle from *Isurus oxyrinchus* (shortfin Mako) was scanned using micro-CT that produced a detailed, three-dimensional denticle. Using CAD software, the denticle was modified slightly to create a symmetric version. The exact same denticle is used in the experimental work of Wen and Lauder,¹⁷ who also provided us with the symmetric CAD model shown in Figure 5. The denticle width is $D_w = 2.4$ s and the height is $D_h = 1.37$ s. The streamwise distance between denticles is $1.032D_w$ and the spanwise spacing is $1.142D_w$. For the staggered case, every other row is shifted half a denticle. In each case, the denticles have been scaled such that $s^+ \approx 16$, which is the near-optimal condition for scalloped riblets. This scaling was chosen to provide the denticles with the best chance of reducing viscous drag and facilitate comparisons with scalloped riblet performance. Finally, the AOI is 13° and is held fixed for all simulated cases.

To make a direct comparison between riblets and sharkskin, we have also simulated scalloped riblets. The domain for the riblet simulation uses a body-fitted curvilinear grid and is shown in Figure 6 on the right. Again, L_y is the characteristic height (from the tips of the riblets to the top of the domain). The riblet case has the same Reynolds number as the sharkskin cases and uses the same baseline case to measure the drag reduction. The riblets have an $s^+ = 16$, an $h/s = 0.5$, and a thickness to width ratio, $t_{95}/s = 0.06$, where t_{95} is defined as the riblet thickness at 95% of the height, h . The riblet computational domain had the same boundary conditions as the denticle simulations.

In order to resolve each denticle with the CURVIB method, a very fine grid is required. Therefore, the background grid is sufficiently fine to ensure that each denticle is locally immersed within a grid resolution with 50 grid points along each spatial direction. To make certain that the background mesh was fine enough to accurately calculate the force on each denticle (as described in Section II), a grid independence study was conducted by doubling the number of grid points in all three directions simultaneously. Due to the large cell counts of the domains, we considered three resolutions (25^3 , 50^3 , and 100^3 grid cells) around a single denticle surrounded by a bed of coarser

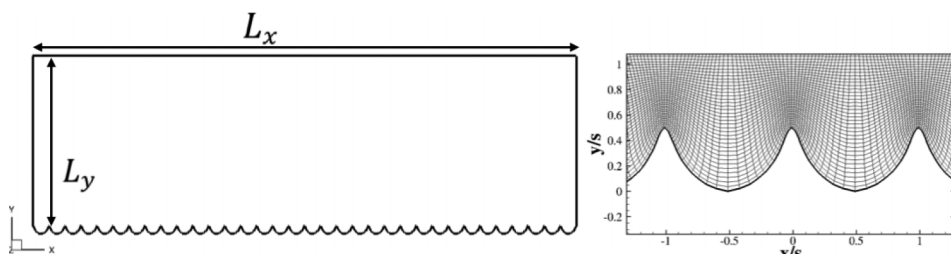


FIG. 6. Right: computational domain with scalloped riblets. Left: the body-fitted mesh for the scalloped riblet.

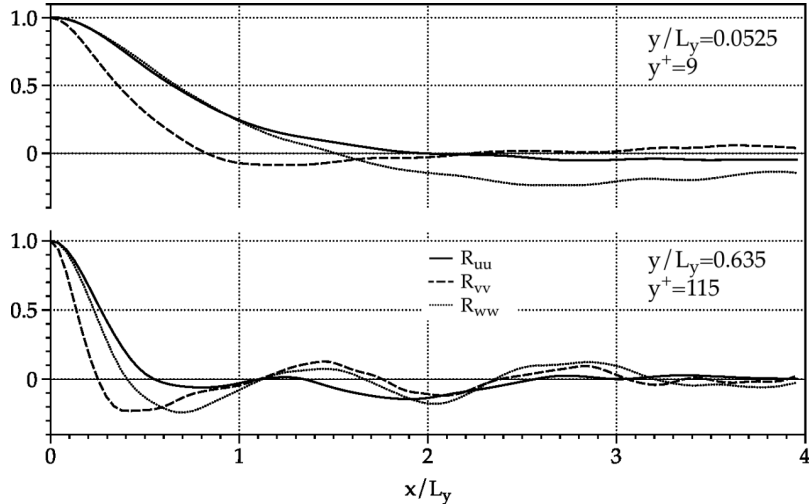


FIG. 7. Two-point correlation in spanwise direction at two separate vertical locations.

resolved denticles in a turbulent channel flow at $Re_\tau = 180$. We found that the resultant force on the highly resolved denticle at 50^3 and 100^3 resolutions varied by just 2%. Based on this study we determined that the 50^3 resolution per denticle is adequate to obtain grid independent solutions. Note that the baseline and riblet cases have geometries that do not vary in the streamwise direction and as such can be modeled accurately with a coarser streamwise resolution of about 7 wall units.

Another set of numerical sensitivity studies was carried out to determine the overall size of the computational domain. Following the approach of Kim *et al.*,²² we sampled velocities from the baseline case and calculated the two-point correlations, R_{ii} , defined in Equation (4), where u'_i denotes the fluctuating velocity in the i th direction ($i = 1, 2, 3, \dots$),

$$R_{ii} = \frac{\overline{u'_i(\mathbf{x}, t) u'_i(\mathbf{x} + \mathbf{r}, t)}}{\overline{u'^2}}. \quad (4)$$

Figures 7 and 8 show that the fluctuating velocities are uncorrelated (i.e., $R_{ii} = 0$) at the boundaries of the computational domain. Figure 7 plots R_{ii} in the spanwise direction, both near the wall

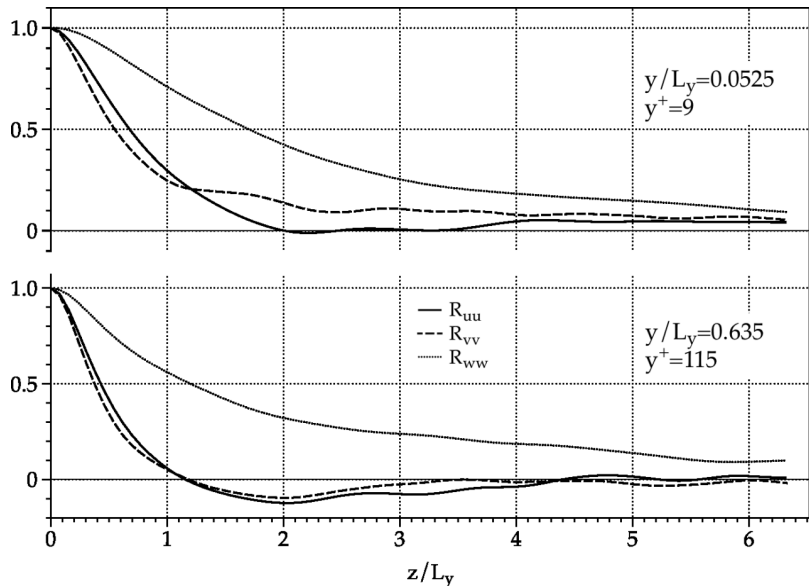


FIG. 8. Two-point correlation in streamwise direction at two separate vertical locations.

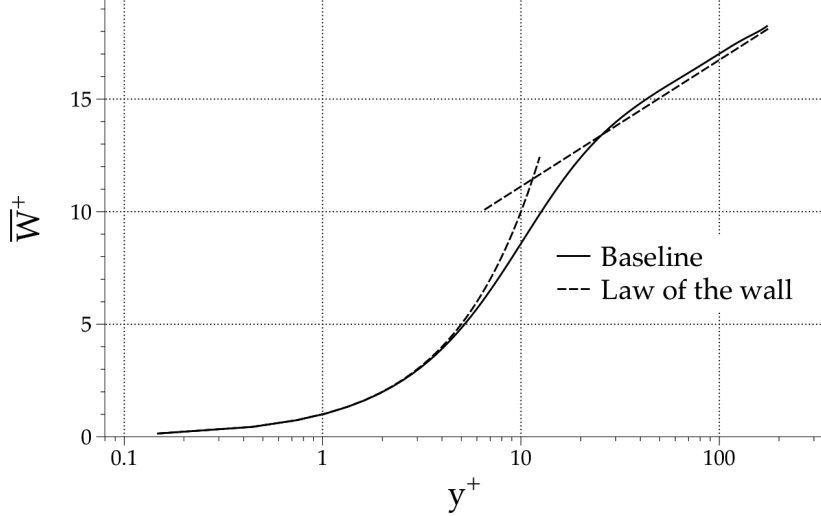


FIG. 9. Mean streamwise velocity for the baseline case obtained from the present DNS. Compared with the law of the wall: $u^+ = y^+$ and $u^+ = 2.44\ln(y^+) + 5.5$.

($y^+ = 9$) and in the logarithmic region of the boundary layer ($y^+ = 115$). Figure 8 shows two-point correlations in the streamwise directions.

IV. VALIDATION OF THE DNS SOLVER

To demonstrate the accuracy of our DNS solver we show in Figures 9 and 10 simulated mean velocity and turbulence statistics profiles for the baseline case (see Table I). As shown in Figure 9 the mean velocity profile is in excellent agreement with the law of the wall. The turbulence statistics profiles in Figure 10 are also in excellent agreement with the benchmark DNS data of Kim *et al.*²²

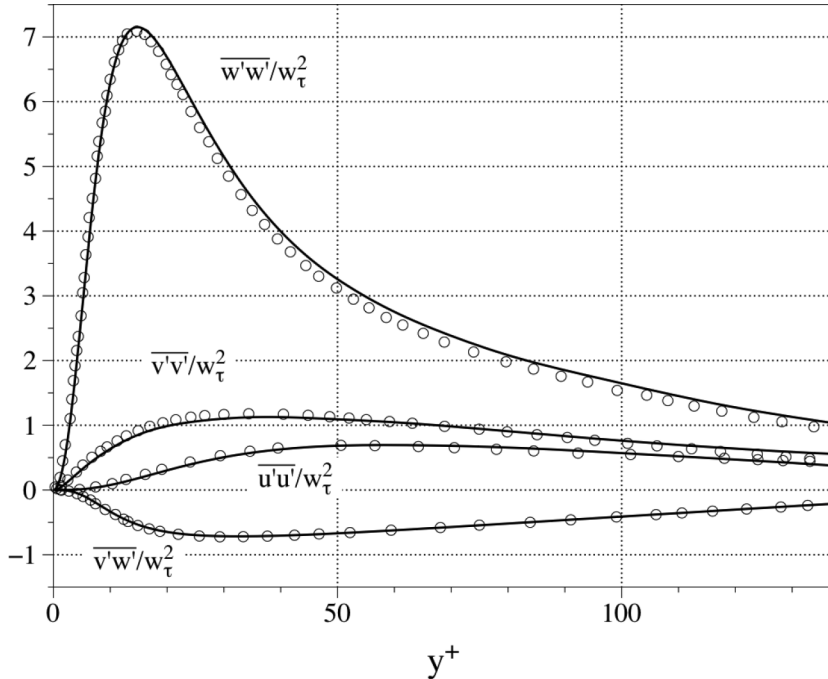


FIG. 10. Left: Present baseline case DNS results (lines) for the Reynolds stresses, compared with the DNS of Kim *et al.*²² (circles). Right: Power spectral density of streamwise velocity fluctuations at a point $y^+ = 36$ from the baseline case.

V. RESULTS AND DISCUSSION

A. Global drag measurements

There are two types of drag created by the denticles: viscous drag and form drag. The form drag is due to pressure differences upstream and downstream of the denticle. The viscous drag is due to the velocity gradient very near the denticle. There is an additional viscous drag due to the membrane to which the denticles are affixed. Therefore, the total drag in the staggered and aligned cases, F_{total} , is

$$F_{total} = F_m + F_p + F_v,$$

where F_p is the pressure drag, F_v is the viscous drag, and F_m is the membrane drag. The baseline and riblet cases incur only viscous drag. Figure 11 is a plot that shows the ratio between total drag with and without sharkskin (and with/without riblets). For comparison, we have included experimental data from Bechert and Reif.¹¹ In Figure 11, the open symbols (and their curve fits) correspond to the experimental sharkskin data at two different values of AOI, 5° and 10°. First, notice that the sharkskin denticles for both staggered and aligned arrangements increase total drag by 45%-50%. These results match very well with the experimental data at $s^+ = 16$, especially considering that the present denticles have an AOI of 13°. Our simulations support the trend that as the AOI increases, so does drag augmentation by sharkskin. In sharp contrast, the scalloped riblets reduce drag in comparison with the baseline. Here too, excellent agreement with the experimental data is achieved, with a drag reduction of 5.2%. It is clear that in both arrangements, sharkskin does not reduce skin friction like riblets, even if the keels are sized at a near optimal value of s^+ . Also, note that the staggered case increases drag more than the aligned case, which will be discussed in more detail in the upcoming results.

Table II shows the calculated contributions of the various components of drag to the total drag for the two denticle cases. For both cases, the contribution of the membrane drag is negligible and can be ignored. Viscous drag is the primary contributor to total drag accounting for approximately 75% of the drag force. A significant contribution to the drag also arises from pressure, which suggests the presence of separated flow among the denticles. The physical reasons for these relative contributions of pressure and form drag will be discussed later in this paper when we will present the three-dimensional structure of the flow in the vicinity of the denticles.

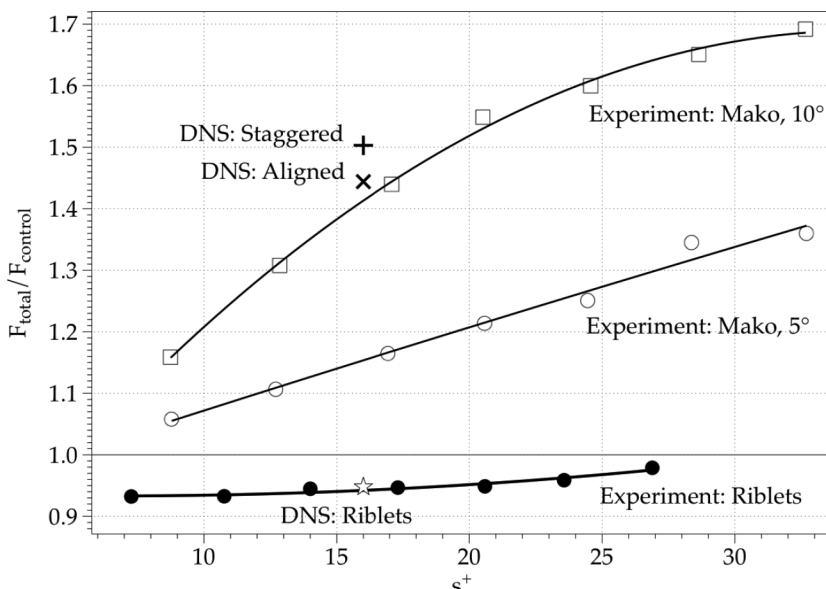


FIG. 11. Ratio between total drag with and without sharkskin (and with/without riblets) from the present DNS. Fitted curves, open squares/circles, and filled circles are experimental data from Bechert *et al.*¹¹ The + and × mark our DNS data for the staggered and aligned denticle cases, respectively. The open star is the present DNS result for the riblets.

TABLE II. Calculated percentage of total drag for the two simulated denticle cases.

Case	F_P (%)	F_v (%)	F_m (%)	F_{total} (%)
Aligned	23.5	76.2	0.3	100
Staggered	26.35	73.5	0.15	100

B. Mean streamwise velocities and turbulence statistics

In this section, we present figures of mean streamwise velocities and turbulence statistics for sharkskin and riblet cases. For the sharkskin profiles, we have not preserved spanwise or streamwise variations in these profiles because we have spatially averaged over the lengths, L_z and L_x . For the riblet case however, we have conditionally averaged the flow in the spanwise direction (i.e., the flow is averaged on a per-riblet basis) and also averaged over L_z . In the spanwise direction, riblet profiles are taken at the riblet tip. The mean streamwise velocities have been normalized with a case-specific shear velocity, w_τ^* , which is defined as

$$w_\tau^* = \sqrt{F_D / \rho A_{fp}}$$

where F_D is the total drag force for each case and A_{fp} is a flat-plate area for each case (i.e., surface area without denticles or riblets). This choice of shear velocity shows the effect of roughness in the logarithmic region. For the turbulence statistics, we have normalized fluctuating velocities with $w_{\tau,0}$, the baseline shear velocity to make direct comparisons among the cases.

In Figures 12–15, we plot mean velocity and turbulence statistics profiles in wall coordinates. We note that in all these figures, the location of the zero-velocity plane, $y = y_0$, varies for each simulation. For the baseline case, $y_0 = 0$ and the origin is the wall. For the denticles, y_0 is defined as the denticle height, D_h . Finally, for the riblet case, y_0 is the riblet peak. Figure 12 shows mean streamwise velocity profiles plotted in wall-coordinates. Obviously, both denticles and riblets greatly alter the turbulent boundary layer by acting to retard the mean flow near their surfaces. Both the baseline and riblet cases exhibit clearly visible logarithmic regions. For the sharkskin case, on the other hand, the logarithmic region is also present but it is shorter and originates further away from the wall as compared to the baseline and riblet cases. To quantify the effective roughness height for the riblet and denticle cases, we formulate the law of the wall as follows:

$$1/\kappa = (\bar{w}/w_\tau^*) / \ln \left(\frac{y - y_0}{k_0} \right). \quad (5)$$

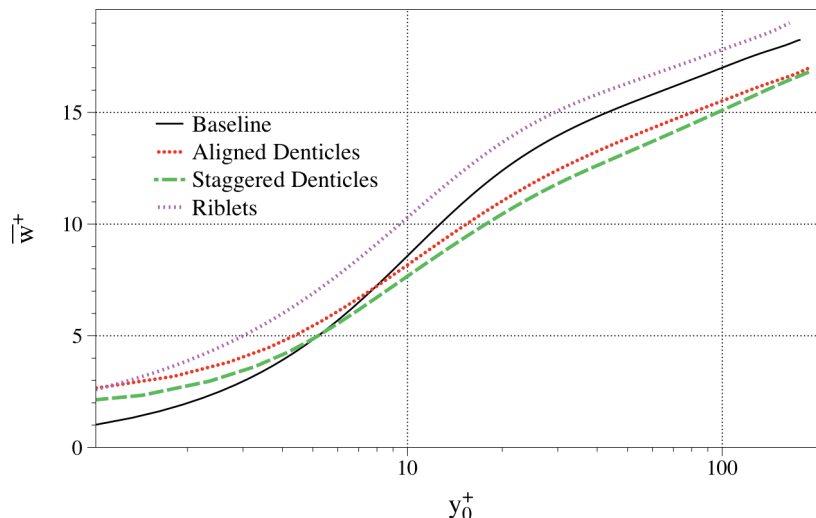


FIG. 12. Mean streamwise velocity normalized with w_τ^* .

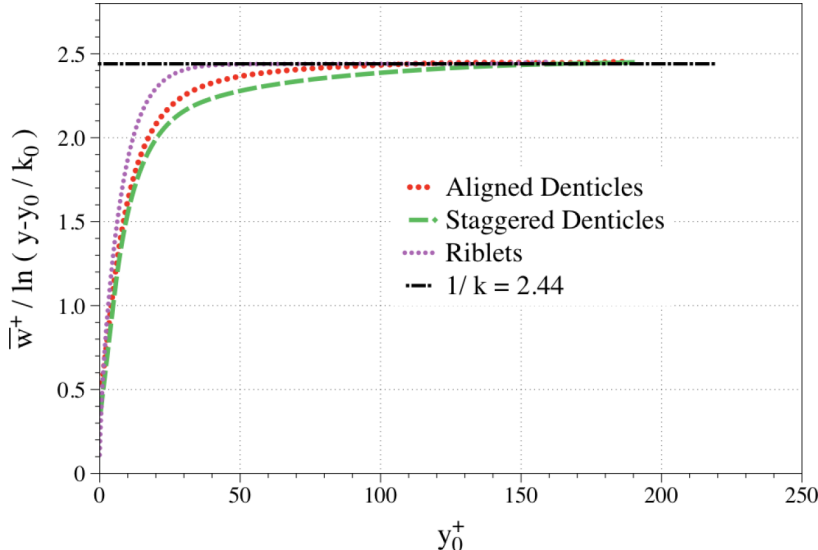


FIG. 13. Equation (5) is plotted for each denticle arrangement and riblet case and used to determine the equivalent roughness height for each case. In the logarithmic region, the profiles overlap with the inverse of the Von Kármán constant.

In the above equation, κ is the Von Kármán constant and k_0 is the effective roughness height. Assuming that both the riblet and denticle mean velocity profiles must satisfy the above equation for the standard value of the Von Kármán constant ($1/\kappa = 2.44$), Equation (5) can be used to determine the effective roughness height k_0 for each case. As shown in Figure 13, the function defined in Equation (5) asymptotes to the standard $1/\kappa$ value for $k_0 = 7(10)^{-4}, 1.9(10)^{-3}, 1.9(10)^{-3}$ for the riblet, denticle staggered, and denticle aligned cases, respectively. Using the relation $k_s = 0.033k_0$ from Jiménez,²³ the roughness height in wall units ($k_s^+ = k_s w_\tau^*/\nu$) for each case is 1.8, 6.2, and 6.2 for the riblet, denticle staggered, and denticle aligned cases, respectively. The riblet case is hydrodynamically smooth, though because of their drag-reducing properties, the skin friction is decreased. On the other hand, the sharkskin is transitionally rough, and their higher values of roughness height correspond with increased skin friction.

Normalized streamwise fluctuations have been plotted in Figure 14, which illustrates that each sharkskin case creates a drastic increase in streamwise fluctuations. Such behavior is the exact opposite of what is seen for the scalloped riblets, which cause a considerable reduction in the streamwise turbulence intensity as compared to the baseline case. Physically, increased statistics

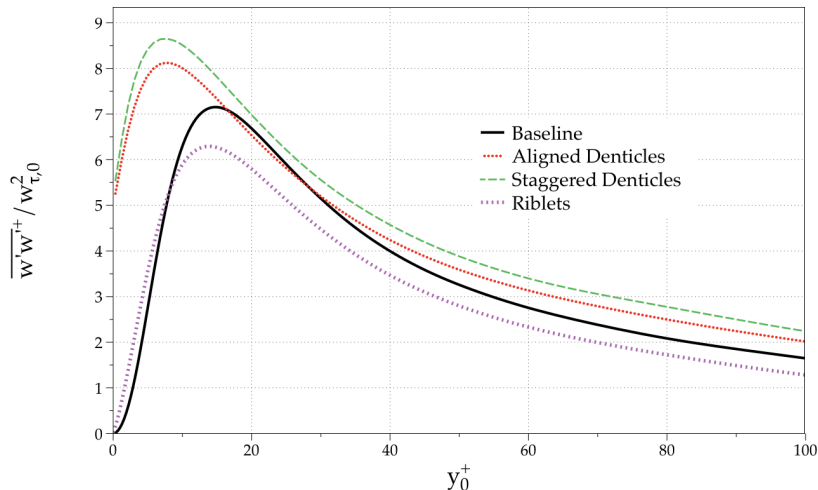


FIG. 14. Streamwise Reynolds stress profiles normalized with $w_{\tau,0}$.

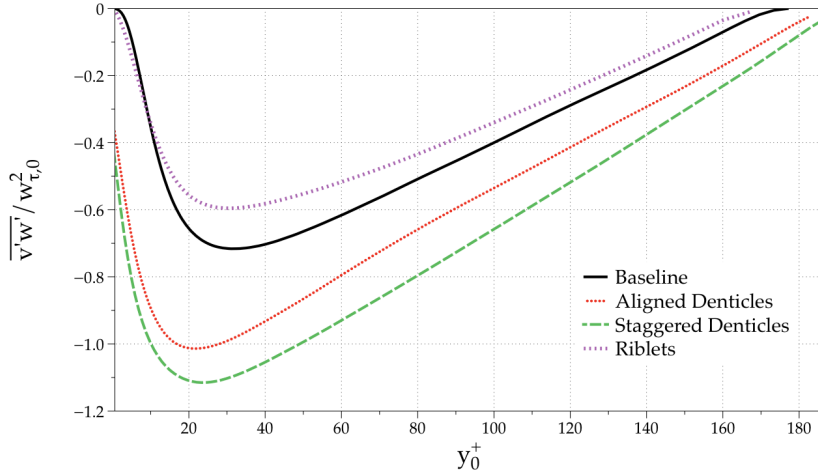


FIG. 15. Primary Reynolds shear stress profiles normalized with $w_{\tau,0}$.

imply increased turbulent mixing and more efficient transport of high-speed outer fluid toward the wall, which, as shown in Figure 11, coincides with increased skin-friction. Similar trends are also observed in Figure 15, which shows the primary Reynolds shear stress profiles for the various cases. Riblets lead to a reduction in Reynolds shear stresses, but for arrangements of denticles, the maximum stress is greatly increased implying increased turbulent mixing consistent with the drag increasing action of denticles.

C. Three dimensional mean flow fields

In order to determine why the two sharkskin arrangements increase drag, time-averaged velocity fields are conditionally averaged in the streamwise and spanwise directions. Conditional averaging is implemented herein by averaging over a patch of denticles, which is specific to each arrangement. The patch we employ for each case is shown in Figure 16. This figure shows mean shear velocity on the membrane with corresponding limiting streamlines. For the aligned denticles, a line of convergence forms at the crown of each denticle suggesting three-dimensional separation and vortex formation. For the staggered case, on the other hand, a saddle node forms upstream of each denticle and the associated pattern of limiting streamlines resembles that of a horseshoe vortex

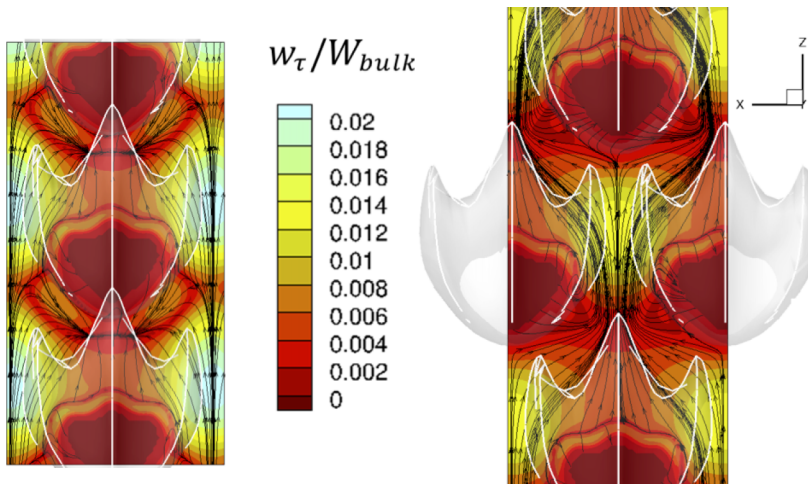


FIG. 16. Streamlines (black lines with arrows) and contours of conditionally averaged shear velocities on the membrane for the aligned case (left) and the staggered case (right). The white lines are used to outline the geometry of the denticles.

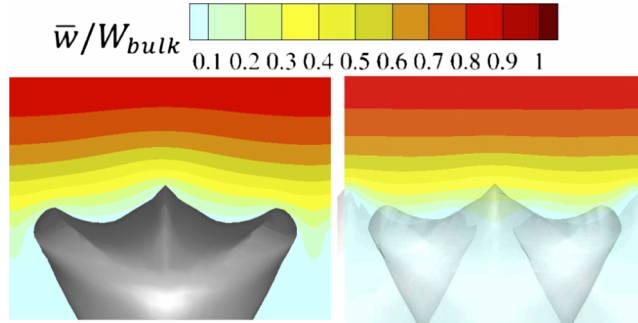


FIG. 17. Mean streamwise velocity at a transverse plane that bisects the denticle for the aligned case (left) and the staggered case (right).

(see Paik *et al.*²⁴). Two stagnation points exist for the aligned case though, one on either side of each denticle. For this case, the overall patterns of the limiting streamlines further suggest that much of the flow is channeled between columns of denticles giving rise to streaks of high shear velocities. In the staggered case, this channeling cannot occur because flow stagnates at the crown of the next denticle. In contrast, for the aligned case each denticle is in the wake of another, which causes separation at the crowns. Finally, the aligned case shows a small region of reverse-flow, which, however, is apparently not enough to cause any type of drag reduction. Staggered denticles incur no mean recirculation anywhere on the membrane.

Figure 17 plots contours of mean streamwise velocity at the transverse plane that bisects a denticle for the aligned and staggered cases. The primary difference between the two cases is the increased velocities at the outer keels for the aligned (left side) arrangement. This too is evidence of flow channeling between denticle columns. Later in this section we will show that flow channeling increases skin-friction on the outer keels of the denticles. In contrast, the staggered case shows no signs of channeling.

The limiting streamline plots suggest three-dimensional separation and vortex formation around the denticle. To further elucidate the structure of the so-induced secondary flow, we plot in Figure 18 averaged non-dimensional vertical velocity contours for the aligned denticle case. This figure reveals a number of interesting trends and highlights the three-dimensional structure of the flow. We note in this figure the strong positive vertical velocity near the crowns, a region of equally strong negative vertical velocity near the outer keels, and a pocket of positive vertical velocity at the ridge of the primary keel. These patterns in the vertical velocity field are suggestive of the presence of counter-rotating streamwise vortices in the mean flow. This feature of the flow is confirmed in Figure 19 where we show iso-surfaces of normalized mean streamwise vorticity.

The presence of coherent, counter-rotating vortices is clearly evident in this figure. Furthermore, the figure also reveals that the formation of the vortex tubes is the result of three-dimensional

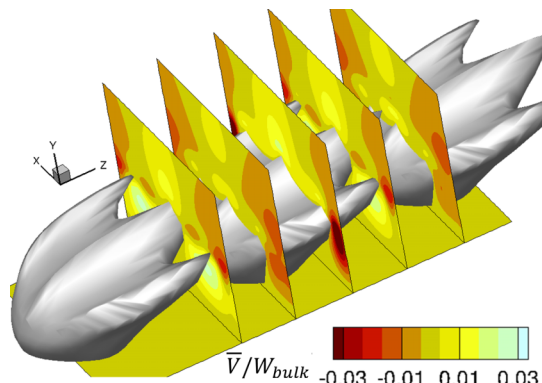


FIG. 18. Mean vertical velocity at several streamwise planes for the aligned denticle arrangement.

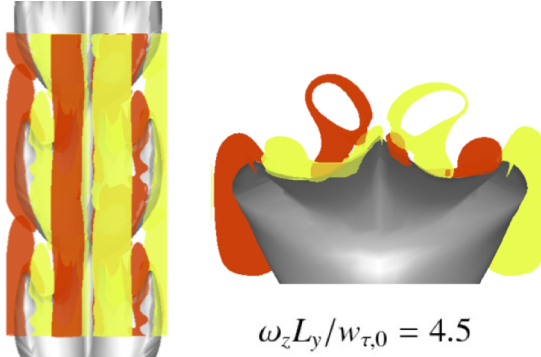


FIG. 19. Iso-surfaces of positive (yellow) and negative (orange) mean streamwise vorticities for the aligned arrangement.

flow separation at the tip of each keel. The interaction of the primary counter-rotating vortices with the surface of the denticles causing the extraction of wall vorticity of opposite sign is also evident from this figure. Finally, we also note the large region of vorticity on the undersides of the denticles. The so resulting complex three-dimensional flow appears to be the main culprit for increasing the mean shear on the denticles.

It is important to note, however, that riblets also induce coherent counter-rotating streamwise vortices but in stark contrast with denticles, reduce drag. To quantify the differences between the two cases, we plot streamwise vorticity contours at a transverse plane in Figure 20 for the riblet and aligned sharkskin cases. As shown in this figure, for both the riblet and denticle cases the magnitude and direction of the counter-rotating vortices are similar, but there is one major difference. Namely, for the drag-reducing riblets the valley between riblets exhibits very low velocity gradients and consequently low shear stress. This is important because Lee and Lee⁶ showed that as s^+ increases, the center points of the streamwise vortices migrate laterally downward into the valley of the riblet, eventually destroying any drag-reducing property. Essentially, this also appears to be the case for the aligned denticles. That is, the valley between the keels of the denticles is not free from vorticity, causing a drag increase rather than reduction. This trend should be attributed to the geometry of the outer keels of the denticles, which are rounded and much shorter than the primary ridge.

Streamwise vorticity contours are also plotted for the staggered denticle arrangement in Figure 21. As shown in this figure, the vorticity field is quite complicated for the staggered case as the vorticity field alternates in a periodic manner in the streamwise direction between positive and negative. To help visualize this complex structure, we also include in Figure 21 vorticity contours on a wall-normal, streamwise plane. It is evident from this figure that a region of negative vorticity originates at the furthest upstream denticle at the crown and continues at the angle of incidence atop a region of positive vorticity created by the crown of the next downstream denticle. It is clear,

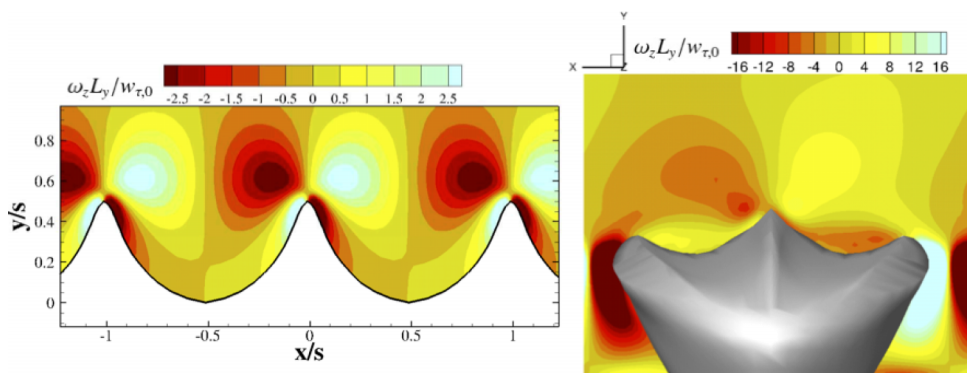


FIG. 20. Front view of mean streamwise vorticity for the scalloped riblets (left) and aligned denticle arrangement (right).

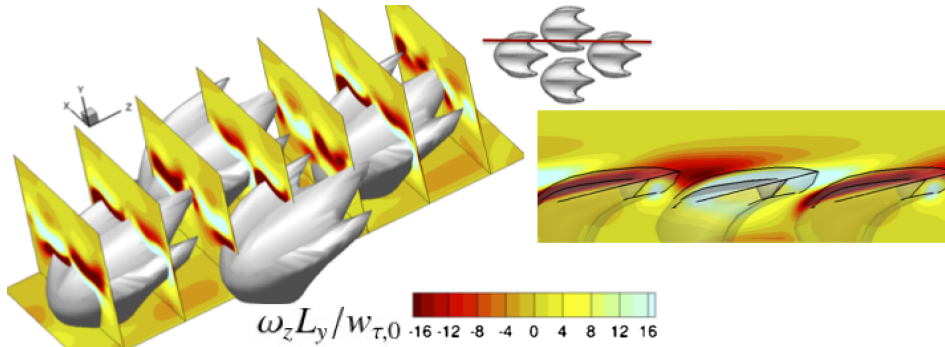


FIG. 21. Isometric (left) and side (right) views of mean streamwise vorticity for the staggered arrangement. Inset shows the spanwise location of side view.

therefore, that the staggered denticle arrangement creates alternating vorticity that two-dimensional riblets can never induce.

The three-dimensional and alternating structure of the resulting streamwise vorticity field for the staggered case, is shown in Figure 22 where we plot positive and negative iso-surfaces of mean vorticity. The resulting structure of the vortices is drastically different than that of the aligned denticles. Individual vortex tubes are not sustained in the streamwise direction, but instead extend for about the size of a denticle. Also, notice that the vortex tubes in this case trend away from the primary keel.

The alternating pattern shown in Figure 22 can be further explained by examining the force components on the denticles. Figure 23 shows contours of the transverse force, F_x , projected onto the denticles for each arrangement, calculated as was described in Section II. The resulting stresses from each denticle were then averaged over all denticles to result in one representative denticle for each case.

In Figure 23, we observe that for the staggered denticle arrangement, the flow is forced away from the primary keel, but for the aligned arrangement, just the opposite occurs—the flow tends toward the primary keel. Thus, while in the aligned case, mean counter-rotating vortices are sustained by the denticles, the staggered arrangement locally changes the direction of the flow at every row of denticles, which prevents sustained counter-rotation. Limiting streamlines plotted on the aligned denticles in Figure 24 highlight a node of reattachment near the outer keels, forcing fluid toward the primary keel. For the staggered case, the stagnation point at the primary keel forces fluid toward the outer keels. Another critical physical insight from the limiting streamlines is that there is a secondary flow on the outer keels. The three-dimensionality of the sharkskin seems to be an inherent disadvantage from a drag-reducing point of view. Drag reduction by riblets is achieved by creating a laminar-like flow velocity gradient on as much wetted area as possible. In both denticle arrangements, however, three-dimensional separation, vortex formation, and strong secondary flow are generated on much of the wetted surface, even in the valleys (between keels), causing a significant augmentation of skin friction drag.

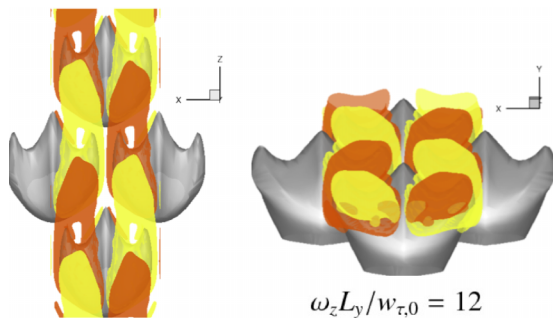


FIG. 22. Iso-surfaces of positive (yellow) and negative (orange) mean streamwise vorticity for the staggered arrangement.

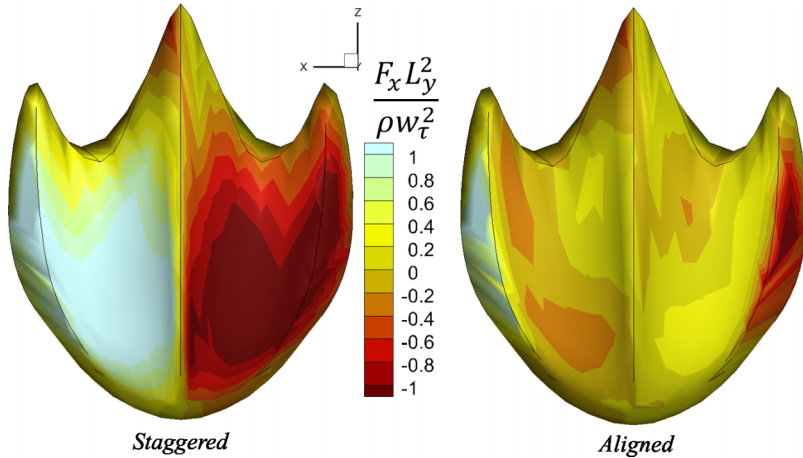


FIG. 23. Normalized spanwise force on a representative denticle (results averaged over all denticles) from the staggered (left) and aligned (right) cases.

The consequence of such secondary flow is evident from plots of mean shear stress magnitude contours shown in Figure 25 for denticles and riblets. Note that Choi⁸ used DNS to show differences in flow fields between drag-reducing and drag-augmenting riblets. One fundamental difference between those two riblets was that the drag-reducing riblet was able to consolidate high shear stress near the riblet peaks. Indeed, our riblet simulation shows a similar result. The riblet tips experience a local shear stress about four times that of the baseline, but the riblet valleys have a much lower value of about half as much as the baseline. It is obvious from the shear stress contours on the denticles that both sharkskin arrangements are unable to consolidate high shear in narrow bands, as between keels, the stress is about equal to the baseline. Finally, it is evident from Figure 26 that for both denticle cases regions of high shear stress are also seen on the sides and undersides of the outer keels. The three-dimensionality of the denticle adds a surface area that is exposed to high shear in ways two-dimensional riblets would not.

D. Comparison with experimental observations

First, we reiterate that the denticles in the present simulations were static and cannot be compared to the experimental findings of Oeffner and Lauder,²⁵ who mounted denticles on a flexible

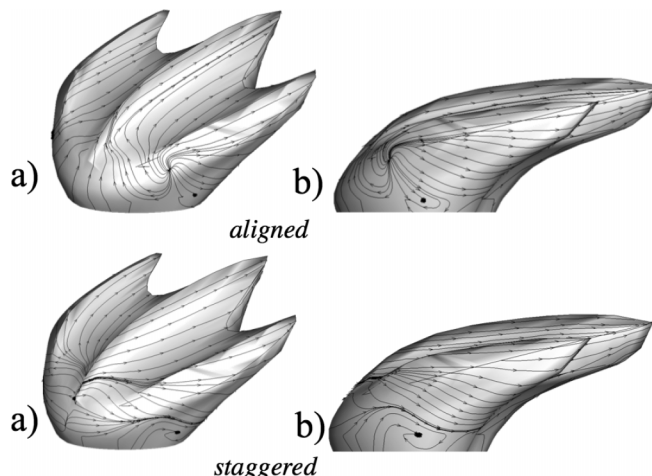


FIG. 24. Mean limiting streamlines on a single denticle from the aligned (top) and staggered (bottom) cases. (a) Isometric view. (b) Side view.

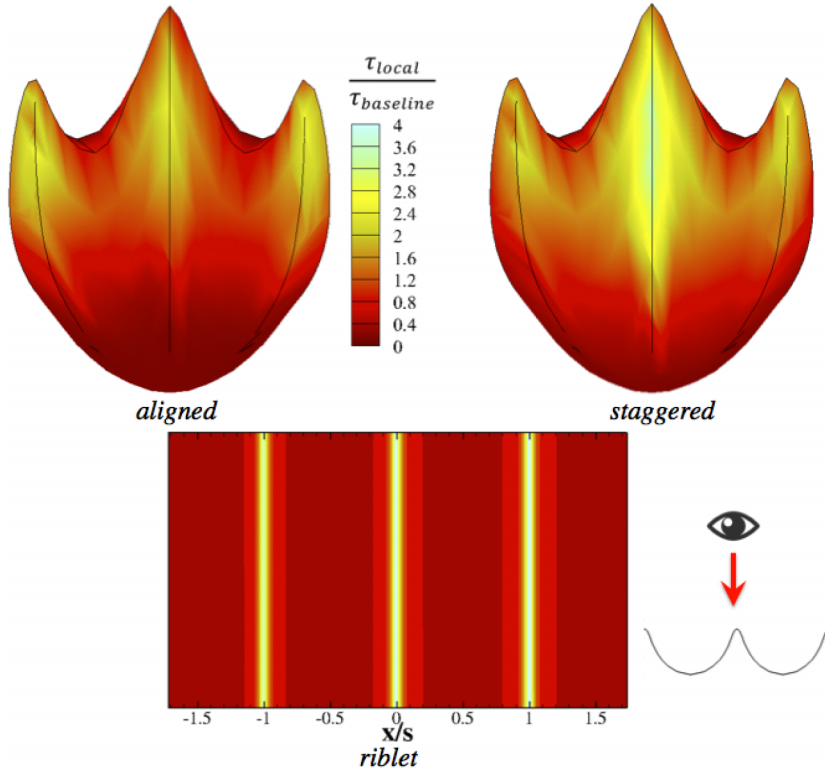


FIG. 25. Contours of time and space averaged shear stress for the aligned (top left) and staggered (top right) denticle arrangements. Similar contours are plotted for the scalloped riblets (bottom).

plate and reported a positive hydrodynamic effect, that is, the primary goal of this work is to systematically compare riblets and sharkskin in the same turbulent flow environment. Second, we note that the present results do not support the experimental findings of Wen and Lauder,¹⁷ who investigated the hydrodynamic effect of static denticles. Their experimental results indicated that the aligned arrangement reduced skin friction, similarly to riblets, up to a maximum of 9%. We argue that the major difference between the work of Wen and Lauder¹⁷ and our study should be attributed to different flow conditions between the simulated and experimental flow fields to which the sharkskin was exposed. In the present work, the denticles are immersed in a canonical fully developed turbulent channel flow. This was not the case in the experiments of Wen and Lauder¹⁷ who exposed denticles in a developing boundary layer flow—the characteristics of which cannot be easily defined. This is an important point because the skin friction relations used by Wen and Lauder¹⁷ to determine s^+ of the sharkskin are only valid for flat plate, fully developed, zero-pressure gradient turbulent boundary layers. Another flow condition that could not be matched between the two cases is the Reynolds number ($Re = 2800$ for the present work and $Re \approx 30\,000$ for Wen and Lauder¹⁷). Although the Reynolds number differs by one order of magnitude, the s^+ values between

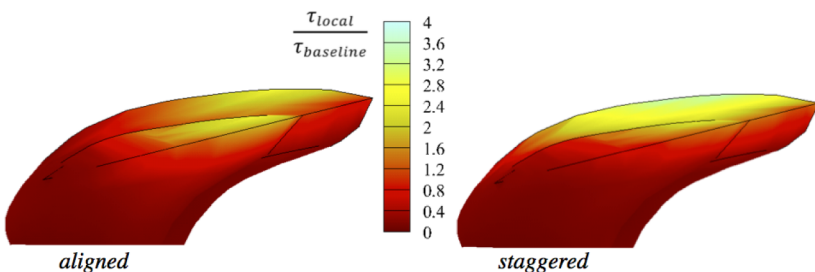


FIG. 26. Contours of time and space averaged shear stress for the aligned (left) and staggered (right) cases.

the experimental and computational studies are similar. According to Bechert *et al.*² matching the s^+ values is an established method for predicting riblet performance. The apparent disagreement between our simulations and the experimental results of Wen and Lauder¹⁷ might suggest that s^+ may not work as well as a scaling parameter for denticles as it does for riblets.

Regardless of the state of the turbulent boundary layer and differences in Reynolds number, Wen and Lauder's¹⁷ sharkskin did reduce drag. The physical reason for this is unknown and cannot be clarified by our simulations since, as discussed above, we could not match their flow conditions in our simulations. The findings of Wen and Lauder,¹⁷ however, considered in conjunction with our results suggest that the hydrodynamic function of sharkskin denticles could depend strongly on the flow conditions to which denticles are exposed.

VI. CONCLUSIONS

Two different arrangements (aligned and staggered) of sharkskin denticles were simulated in a turbulent boundary layer with a sharp-interface immersed boundary method and direct numerical simulation. For direct comparison, scalloped-shaped riblets were also simulated. The Navier-Stokes equations were solved with a finite-difference, fractional-step method that was fourth-order accurate in time and second-order accurate in space. Due to our method and high-resolution background mesh, detailed flow fields were obtained around individual denticles. This is the first time that such detailed simulations for actual denticle shapes have been reported.

Compared to a flat plate without sharkskin, an aligned denticle arrangement increased total drag by 44%, and a staggered increased total drag by 50%. On the other hand, the riblets decreased drag by 5.2%. Even though denticles resemble riblets, we have found that the three-dimensionality of the denticle geometry enhances turbulent mixing and increases skin-friction. More specifically, there are several key differences between denticles and drag-reducing riblets.

1. 25% of total denticle drag is attributable to form drag, due to separation around individual denticles. Riblets have no form drag.
2. Significant secondary flow is present along the outer keels and even under the keels of denticles.
3. The denticles significantly increase the Reynolds stresses. Riblets decrease these statistics.
4. Riblets induce steady counter-rotating vortices on either side of the peaks, but only for the aligned case such vortices are seen for denticles.
5. Riblets isolate high mean shear stress to peaks, but denticles are unable to do so; denticle valleys are areas of high shear stress and in both cases, the entire primary keel is exposed to high velocity gradients.

Our results have conclusively shown that the three-dimensionality of the denticles causes a secondary flow that is the cause of drag increase. As a result, the present simulations support the experimental evidence of Reif and Bechert.¹¹ In conjunction with the experimental findings of Bechert *et al.*,¹⁴ our results suggest that sharkskin denticles will only function as riblets if the denticles interlock. Most importantly, for sharkskin to reduce skin friction like riblets, they must be sized correctly, and this is very difficult to know without knowing the shear velocity distribution on a shark.

Notably, in the aligned case, our results do not agree with the experimental study by Wen and Lauder.¹⁷ The cause is likely due to the difference in flow conditions to which denticles were exposed in the experiments and our simulations. The fact that denticles were able to reduce drag in the experiment of Wen and Lauder,¹⁷ however, suggests that further studies are needed to systematically investigate the function of denticles in different flow environments.

ACKNOWLEDGMENTS

This project was made possible by financial support from the Department of Energy and Sandia National Laboratories. Computing resources were provided by the University of Minnesota Supercomputing Institute. We would like to thank the Li Wen and George Lauder for the 3D CAD denticle and their biological insight.

- ¹ W. Raschi and J. A. Musick, *Hydrodynamic Aspects of Shark Scales* (National Aeronautics and Space Administration, Scientific and Technical Information Branch, 1986), Vol. 3963.
- ² D. Bechert, M. Bruse, W. Hage, J. T. Van der Hoeven, and G. Hoppe, "Experiments on drag-reducing surfaces and their optimization with an adjustable geometry," *J. Fluid Mech.* **338**, 59–87 (1997).
- ³ M. Walsh, "Turbulent boundary layer drag reduction using riblets," AIAA Paper No. 82-0169, 1982.
- ⁴ L. Djennidi and R. Antonia, "Laser doppler anemometer measurements of turbulent boundary layer over a riblet surface," *AIAA J.* **34**, 1007–1012 (1996).
- ⁵ S.-R. Park and J. M. Wallace, "Flow alteration and drag reduction by riblets in a turbulent boundary layer," *AIAA J.* **32**, 31–38 (1994).
- ⁶ S.-J. Lee and S.-H. Lee, "Flow field analysis of a turbulent boundary layer over a riblet surface," *Exp. fluids* **30**, 153–166 (2001).
- ⁷ Y. Suzuki and N. Kasagi, "Turbulent drag reduction mechanism above a riblet surface," *AIAA J.* **32**, 1781–1790 (1994).
- ⁸ H. Choi, P. Moin, and J. Kim, "Direct numerical simulation of turbulent flow over riblets," *J. Fluid Mech.* **255**, 503–539 (1993).
- ⁹ D. C. Chu and G. E. Karniadakis, "A direct numerical simulation of laminar and turbulent flow over riblet-mounted surfaces," *J. Fluid Mech.* **250**, 1–42 (1993).
- ¹⁰ D. Goldstein, R. Handler, and L. Sirovich, "Direct numerical simulation of turbulent flow over a modeled riblet covered surface," *J. Fluid Mech.* **302**, 333–376 (1995).
- ¹¹ W. Reif and D. Bechert, "On the drag reduction of the shark skin," in *AIAA Shear Flow Control Conference* (1985).
- ¹² A. W. Lang, M. T. Bradshaw, J. A. Smith, J. N. Wheelus, P. J. Motta, M. L. Habegger, and R. E. Hueter, "Movable shark scales act as a passive dynamic micro-roughness to control flow separation," *Bioinspiration Biomimetics* **9**, 036017 (2014).
- ¹³ B. Dean and B. Bhushan, "Shark-skin surfaces for fluid-drag reduction in turbulent flow: A review," *Philos. Trans. R. Soc., A* **368**, 4775–4806 (2010).
- ¹⁴ D. Bechert, M. Bruse, and W. Hage, "Experiments with three-dimensional riblets as an idealized model of shark skin," *Exp. fluids* **28**, 403–412 (2000).
- ¹⁵ Y. C. Jung and B. Bhushan, "Biomimetic structures for fluid drag reduction in laminar and turbulent flows," *J. Phys.: Condens. Matter* **22**, 035104 (2010).
- ¹⁶ G. Lauder, P. Madden, J. Tangorra, E. Anderson, and T. Baker, "Bioinspiration from fish for smart material design and function," *Smart Mater. Struct.* **20**, 094014 (2011).
- ¹⁷ L. Wen, J. C. Weaver, and G. V. Lauder, "Biomimetic shark skin: Design, fabrication and hydrodynamic function," *J. Exp. Biol.* **217**, 1656–1666 (2014).
- ¹⁸ Y. Saad and M. H. Schultz, "Gmres: A generalized minimal residual algorithm for solving nonsymmetric linear systems," *SIAM J. Sci. Stat. Comput.* **7**, 856–869 (1986).
- ¹⁹ L. Ge and F. Sotiropoulos, "A numerical method for solving the 3d unsteady incompressible Navier–Stokes equations in curvilinear domains with complex immersed boundaries," *J. Comput. Phys.* **225**, 1782–1809 (2007).
- ²⁰ I. Borazjani and F. Sotiropoulos, "On the role of form and kinematics on the hydrodynamics of self-propelled body/caudal fin swimming," *J. Exp. Biol.* **213**, 89–107 (2010).
- ²¹ R. Garcia-Mayoral and J. Jimenez, "Hydrodynamic stability and breakdown of the viscous regime over riblets," *J. Fluid Mech.* **678**, 317–347 (2011).
- ²² J. Kim, P. Moin, and R. Moser, "Turbulence statistics in fully developed channel flow at low Reynolds number," *J. Fluid Mech.* **177**, 133–166 (1987).
- ²³ J. Jiménez, "Turbulent flows over rough walls," *Annu. Rev. Fluid Mech.* **36**, 173–196 (2004).
- ²⁴ J. Paik, C. Escauriaza, and F. Sotiropoulos, "On the bimodal dynamics of the turbulent horseshoe vortex system in a wing-body junction," *Phys. Fluids* **19**, 045107 (2007).
- ²⁵ J. Oeffner and G. V. Lauder, "The hydrodynamic function of shark skin and two biomimetic applications," *J. Exp. Biol.* **215**, 785–795 (2012).